J. Earth Syst. Sci. (2021)130 155
https://doi.org/10.1007/s12040-021-01648-5

Petrogenesis of the Late Archean Kanara Batholith of the Western Dharwar Craton: Evidence for mid-deep crustal recycling of the Archean felsic crust

Jayant K Padhi, Chandan K Boraiaha* and Rashmi Chandan

Ore Research and Exploration (ORE) Group, Department of Geology, Central University of Kerala, Kasaragod, Kerala 671 320, India.
**Corresponding author. e-mail: rcgeo85@icloud.com*

MS received 20 August 2020; revised 30 January 2021; accepted 24 March 2021

Kanara Batholith is an intrusive granitoid pluton into the basement biotite-gneisses and the supracrustal rocks of the Western Ghats Belt (WGB). The pluton is situated in the western margin of the Western Dharwar Craton (WDC). These granitoids are classified as granodiorite and granite based on their field and petrographic characteristics. Based on the abundance and presence of alkali-feldspar phenocrysts, the granites are further classified as porphyritic and non-porphyritic granites. Biotite±amphibole is a dominant mafic mineral phase in the granodiorites, whereas amphiboles are absent in the studied granites. Textural coarsening has played a significant role in the growth of the mineral crystals within the studied granitoids. Thermobarometric study suggests that the granites were emplaced and crystallized at pressures between 4.32 and 4.92 kbar and temperatures between 548±15° and 715±15°C. Further, it is estimated that the granitoid magma intruded the gneissic country rocks and the supracrustal sequences of the WGB corresponding to a depth of ∼15 to 17 km. Geochemical evidence indicates that the source magmas of the studied granitoids were derived from the interaction between (i) a melt derived from the partial melting of the basement biotite gneisses and (ii) a melt derived from the partial melting of the early Archean metasedimentary rocks that form enclaves within the basement biotite gneisses. These two source magmas have interacted subsequently to yield a hybrid felsic magma, resulting in the Kanara Batholith formation. The interaction between the melts took place at shallow to mid-crustal levels at pressures $\lesssim$ 5 kbar before the crystallization began.

Keywords. Kanara Batholith; Dharwar Craton; Western Dharwar Craton; petrogenesis; crustal recycling.

1. Introduction

Progress in understanding the crustal evolution of the Archean cratons has benefitted remarkably from the study of the genesis of felsic magmatic rocks. This is particularly true due to the widespread distribution of the granitoid rocks in the Archean cratons (Condie *et al.* 2009; Condie 2014; Laurent *et al.* 2014). Most models describing the Archean crustal evolution demonstrates that the juvenile accretion was the dominant process during the Eoarchean–Paleoarchean, while the

Supplementary material pertaining to this article is available on the *Journal of Earth System Science* website (http://www.ias.ac.in/Journals/Journal_of_Earth_System_Science).
Published online: 04 August 2021

reworking of pre-existing continental crust became progressively more important from the Neoarchean onwards (Jayananda *et al.* 2019; Dey and Moyen 2020). The juvenile addition and the reworking patterns are evident in the accretion of the tonalite–trondhjemite–granodiorite (TTG) suites and the subsequent potassic granites (Moyen *et al.* 2003; Laurent *et al.* 2014; Ranjan *et al.* 2020). The spatial link between the reworking events and the major thermal events that led to the stabilization of the Archean cratons are very well documented (Jayananda *et al.* 2006; Tait *et al.* 2011; Laurent *et al.* 2014). Despite this, the genetic link between the juvenile and reworked crustal products and their spatial connection with the thermal events and the Archean crustal growth are still under debate (Jayananda *et al.* 2019).

The Dharwar Craton (DC, figure 1) in southern India is an ideal terrain to address the juvenile magma additions and the reworking in the Archean crustal evolution (Dey 2013; Mukherjee *et al.* 2017; Jayananda *et al.* 2019; Mohan *et al.* 2020; Dey and Moyen 2020; Nicoli 2020). The Craton is subdivided into Western Dharwar Craton (also known as Dharwar Foreland; Chadwick *et al.* 2000) consisting of Neoarchean schist belts and older plutonic and supracrustal rocks in the west, and Eastern Dharwar Craton (also known as Dharwar Accretionary Complex; Chadwick *et al.* 2000) dominated by polyphase calc-alkaline plutonic rocks interspersed with relics of intra-arc basins in the east (figure 1; Chadwick *et al.* 2007). A diffused boundary of at least 200 km wide to the east of the Chitradurga Shear Zone (CSZ) marks the limits of the Western Dharwar Craton (WDC) and the Eastern Dharwar Craton (EDC). The Craton division into two blocks is justified in terms of the nature and abundance of schist belts, crustal

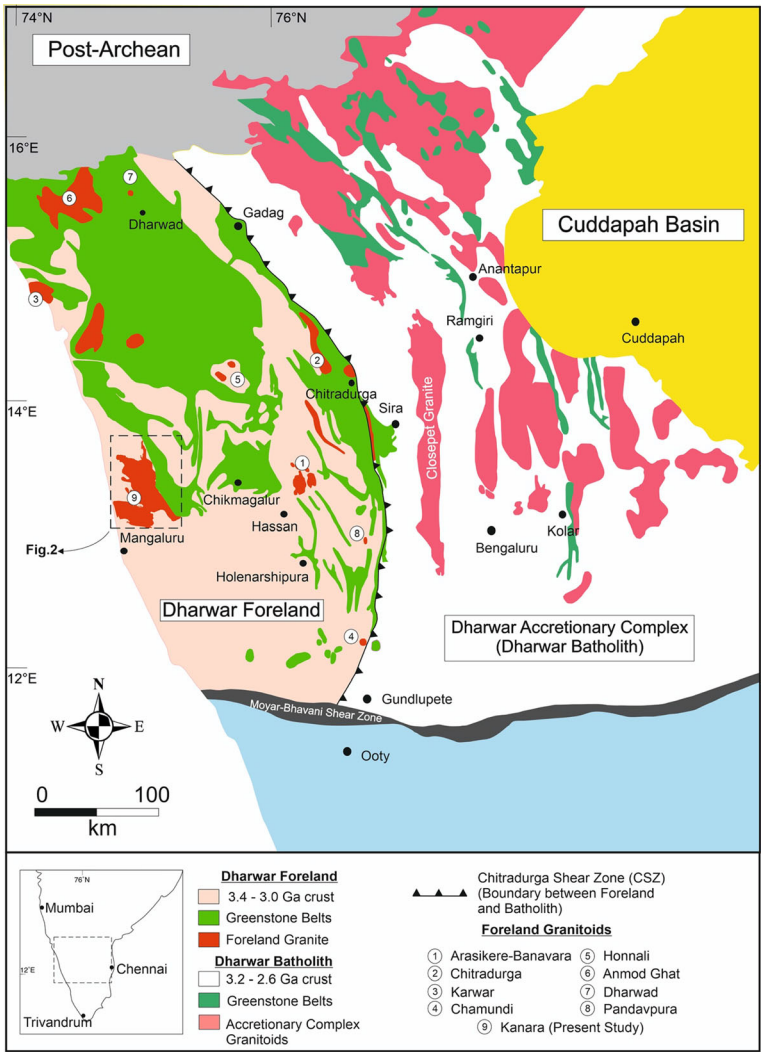

Figure 1. Outline geological map of the Dharwar Craton, southern peninsular India (modified after Chadwick *et al.* 2007; Devaraju *et al.* 2009).

thickness, the grade of regional metamorphism, and degree of melting (Chadwick *et al.* 2000, 2007; Jayananda *et al.* 2013, 2018, 2020). The WDC is dominated by older (3400–3200 Ma) crust while the EDC is dominated by younger (2700–2520 Ma) crust with no significant crustal remnants older than 2700 Ma. The diffuse boundary region in between the WDC and the EDC is significantly characterized by the presence of mixed older (3400–3200 Ma) and younger crust (2700–2520 Ma) (Chardon *et al.* 2011; Peucat *et al.* 2013).

In most parts of the WDC, the granitoid rocks comprise a composite mosaic of plutons which evolved during the middle-late Archean period, from 3.3 to 2.6 Ga (Devaraju *et al.* 2009). The Kanara Batholith granitoid discussed in this paper form part of the western margin of the WDC (figure 1), which stretches over an area of ∼2000 km^2. The northern part of the pluton has been thoroughly studied in this contribution to (i) characterize the pluton relationship with the basement gneisses, and the adjacent Western Ghats greenstone belt (WGB), (ii) decipher its petrogenesis, and (iii) investigate the magma chamber processes.

2. General geology and lithostratigraphy of the study area

The study area forms part of the granite-greenstone terrain and represents mainly middle to deeper Archean crust. The massive Kanara Batholith is surrounded by the biotite gneisses on three sides, while the volcano-sedimentary sequences of the middle to late-Archean Western Ghats greenstone belt (WGB) marks the eastern boundary of the pluton (figures 2, 3a). The significant occurrence of enclaves of the WGB supracrustal rocks along the eastern margin of the pluton (figure 3b) suggests that the pluton forms the basement for the supracrustal rocks. Both the pluton and the greenstone belt are intruded by younger mafic dykes. Enclaves of migmatite gneisses are also not uncommon (figure 3c).

The WGB is dominated by metavolcanic rocks which account for ∼80% of the lithologies followed by metasediments (Ramakrishnan and Vaidyanadhan 2010; Chandan Kumar and Ugarkar 2017). The metavolcanic rocks of WGB vary in composition from mafic to felsic, with the former being distinctly dominant. The mafic volcanic rocks, along with the conglomerates and quartzites, occupy the lower portion, whereas the banded iron formations (BIF) and felsic volcanic rocks occupy the upper part of the stratigraphic sequence (Ramakrishnan and Harinadha Babu 1981; Chandan Kumar and Ugarkar 2017). The oligomict quartz-pebble conglomerate and the associated cross-bedded quartzite appear to have been deposited conformably in the early stages of the basin development. Perhaps, they represent the non-turbulent periods of sedimentation and display a transition from clastic to chemogenic sedimentation. This sedimentation is followed by overwhelming mafic volcanism, followed by a brief period of chemogenic sedimentation, which resulted in the formation of the world-class magnetite deposits (Ramakrishnan and Harinadha Babu 1981). The volcano-sedimentary activity in the belt culminated with the felsic magma eruption in the eastern margin of the belt towards the end of 2.6 Ga (Chandan Kumar and Ugarkar 2017; Ramakrishnan and Harinadha Babu 1981).

There is overall structural conformity between the gneiss and the greenstone belt. Both display NW to NNW planar fabric manifested in their foliation, banding, bedding planes, and fold axial planes. The gneissic foliation trends in an NNW–SSE direction with a general dip of 40°–50° due east, which is similar to the general trend of the schistosity planes of the volcano-sedimentary sequences of WGB. However, the dip reversals are recorded in the gneisses towards the western margin of the Kanara Batholith (figure 2). Similarly, the axial plane of the folds in the gneisses too trend in the NNW–SSE direction. Contrarily, the magmatic flow bands in the granodiorites in the core portion of the pluton exhibit distinct E–W trend. The contact planes between the pluton and the gneisses show NW–SE trends with gentler dips variable from east to west along the pluton margin (figure 2).

The rocks of the WGB and the basement gneisses bear evidence of medium to high-grade metamorphism in the range of upper amphibolite to granulite facies (Ramakrishnan and Harinadha Babu 1981; Ramakrishnan and Vaidyanadhan 2010). No evidence of the impact of this metamorphism on the Kanara Batholith is noticed in the field.

3. Field and mineralogical characteristics

The Kanara Batholith shows significant evidence of its intrusive nature into the surrounding biotite gneisses (figure 3a–c). The contact between the

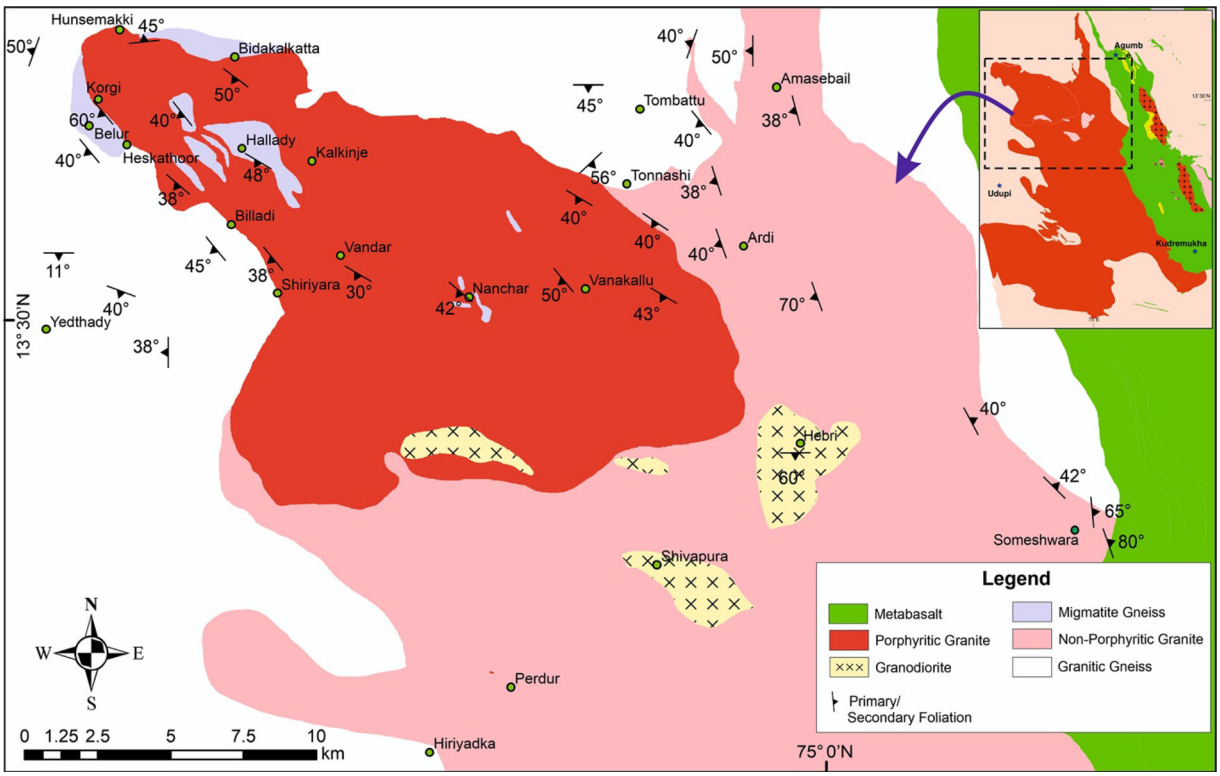

Figure 2. Geological map of the northern part of the Kanara Batholith pluton in the western Margin of the Dharwar Craton (modified after Ramakrishnan and Harinadha Babu 1981).

studied granitoids and the surrounding supracrustal rocks of the Western Ghats belt (WGB) is sharp (figure 3a). Numerous enclaves of schistose metabasalts are common within the undeformed non-porphyritic granites along the eastern contact margin between the granitoids and WGB (figure 3b). Characteristics such as increased migmatization and remarkable enrichment of mafic mineral phases (especially biotite±amphibole; up to 20–30%) proximal to gneiss-batholith contact indicate the intrusive nature of the batholith. The studied biotite gneisses are characterized by (i) the growth of recrystallized plagioclase crystals parallel to the oriented mafic mineral phases and (ii) the elongation of quartz crystals parallel to the gneissic foliation. The gneisses are medium to coarse-grained with the abundance of quartz, plagioclase, alkali feldspar and biotite (figure 3d). Hornblende is present occasionally.

The Kanara Batholith includes two rock variants emplaced within the biotite gneisses: (i) granodiorite and (ii) granite. The granodiorite constitutes a minor part and is mainly confined to the central part of the pluton (figure 2). However, the granite is voluminous and is further classified as porphyritic and non-porphyritic varieties (figure 2).

3.1 *Granodiorite*

The granodiorites occur in the central part of the pluton, in and around Hebri and Shivapura localities (figure 2). They are medium to coarse-grained rocks characterized by equigranular hypidiomorphic texture. The rocks exhibit anhedral to subhedral mineral phases, occasional foliation along the contact and epidotization (figure 3e–f). Numerous microgranular enclaves made up of quartz, plagioclase and K-feldspars are common in the studied granodiorites (figure 3e).

Plagioclase (42%), quartz (24%), alkali feldspar (18%), biotite (13%) and hornblende (5%) are the dominating mineral phases (figures 4a and 5). The accessory minerals include zircon, allanite, titanite, apatite and magnetite. The alkali feldspars are mostly microcline and are occasionally perthitic (figure 4b). The coarser alkali-feldspars usually contain full or partial inclusions of plagioclase and biotite. Myrmekitic intergrowth of feldspar crystals and the development of sericite due to alteration of plagioclase are not uncommon. Primary biotite mantling hornblende is a usual phenomenon. Occasional replacement of hornblende crystals by biotite is not uncommon.

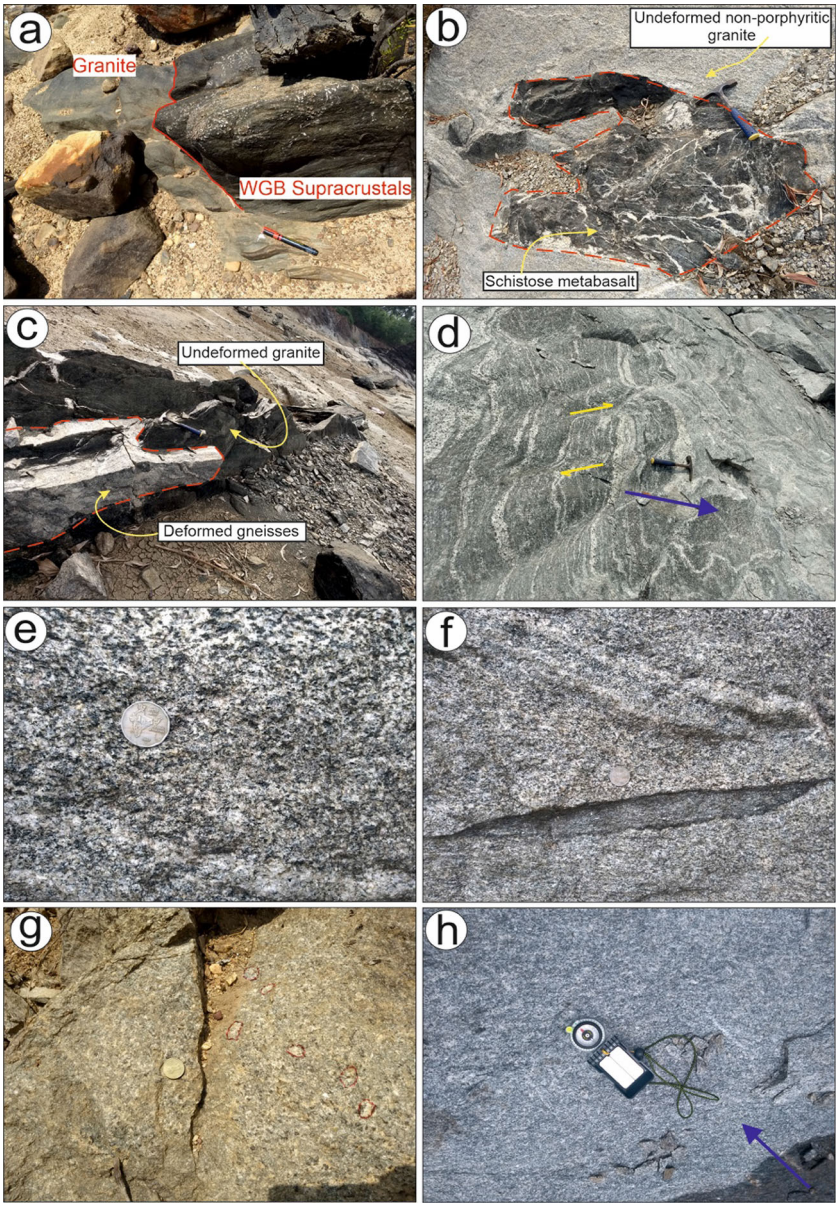

Figure 3. Field photographs. (**a**) Contact between the studied non-granites and the supracrustal rocks of the Western Ghats Belt (WGB); (**b**) enclave of schistose metabasalt within the undeformed non-porphyritic granites along the eastern contact margin between the Kanara Batholith and the WGB; (**c**) enclave of migmatitic gneisses within the undeformed porphyritic granites along the north-western contact margin between the Kanara Batholith and the basement biotite–gneisses; (**d**) sheared biotite–gneisses along the eastern margin of the batholith; (**e**) granodiorite outcrop in the center of the batholithic pluton (near Shivapura village); (**f**) microgranular enclave (consists mainly of quartz, plagioclase and K-feldspars) within the granodiorite; (**g** and **h**) porphyritic granite and non-porphyritic granite variants, respectively.

3.2 *Granite*

Granites make up about ∼80 to 90% of the Kanara Batholith area, followed by granodiorite and small patches of migmatitic gneisses. The typical porphyritic variant of the granites is confined to the northwestern part, while the non-porphyritic granite variant occupies most of the pluton (figure 2). The boundary between the two variants is gradational and spans across 2–3 km.

3.2.1 *Non-porphyritic granite*

The non-porphyritic granitic rocks are equigranular, hypidiomorphic and, in most cases, show a weak primary foliation exhibited by the planar arrangement of felsic minerals (figure 3h). The rocks are coarse-grained, and the mineral crystals are usually anhedral. Quartz (38%), plagioclase (28%), alkali feldspars (25%) and biotite (9%) are the dominating mineral phases (figure 5).

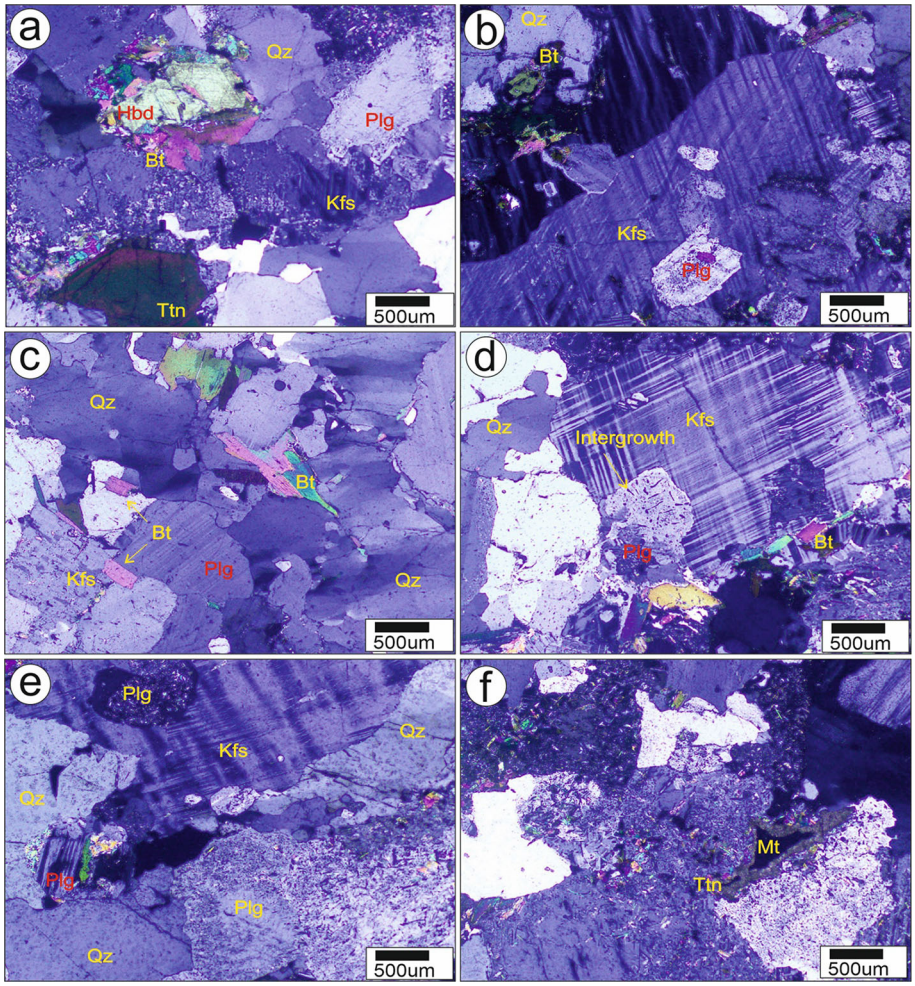

Figure 4. Photomicrographs of the studied granitoids. (**a**) Granodiorites, note the biotite mantling hornblende and a titanite crystal in the lower left corner; (**b**) perthitic alkali-feldspar hosting plagioclase crystal in granodiorites; (**c**) microcline alkali feldspar hosting plagioclase crystal as well as showing mutual intergrowth relationship; (**d**) perthitic alkali-feldspar associated with plagioclase in non-porphyritic granites. Note the quartz and biotite inclusions in plagioclase and alkali feldspar; (**e**) microcline containing poikilitic plagioclase crystal and inclusion of biotite in porphyritic granite; (**f**) titanite mantling magnetite in porphyritic granite.

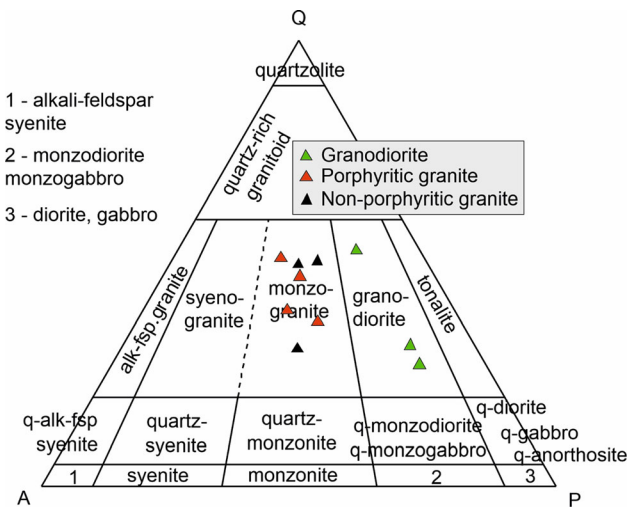

Figure 5. QAP classification diagram of Kanara Batholith granitoids (Streckeisen 1974).

Accessory mineral phases include zircon, magnetite and apatite. Alkali feldspars are predominantly microcline. Hornblende is occasionally present. Similar to the granodiorites, the feldspars usually carry inclusions of biotite crystals (figure 4c–d).

3.2.2 *Porphyritic granite*

The presence of euhedral alkali-feldspar phenocrysts characterizes the porphyritic granites. The longest axis of the phenocrysts varies between 2 and 5 cm (figure 3g). The matrix is composed of coarse-grained quartz, plagioclase and microcline. The mafic mineral phases include biotite and magnetite. Allanites, ranging in size between 0.5 and 1 cm, are often found as an accessory mineral phase in the porphyritic granites. The longer axis

of the microcline phenocrysts shows a strong alignment in NNW–SSE direction due to the melt supported deformation. Migmatitic gneisses often occur as huge enclaves (figure 3c), while pegmatitic dykes, quartz and aplitic veins are often seen cross-cutting these granites.

The mineral crystals are subhedral to euhedral in shape. Quartz (33%), alkali feldspar (32%), plagioclase (31%), and biotite (6.87%) are the dominating mineral phases (figure 5). The accessory mineral phases include zircon, apatite, allanite, titanite and magnetite. The microcline phenocrysts usually contain plagioclase and biotite inclusions (figure 4e). The porphyritic granites also contain magnetite minerals mantled by titanite (figure 4f). Myrmekitic intergrowth of feldspars and titanite mantling magnetite is common in the studied granites.

4. Analytical methods

4.1 *Crystal size distribution*

The crystal size distribution (CSD) is a quantitative textural analysis tool that Larson and Randolph (1971) first developed to study industrial crystallization processes. The usage of the technique in petrology was developed by Marsh (1988) and Cashman and Marsh (1988). The parameters used are the crystal sizes (maximum length, maximum width and area) plotted with their population density in a log–log scale. The curves hence produced indicate the nucleation and growth rates. Specific patterns also correspond to various igneous processes that resulted in the formation of the crystals and the enclosing rock as they are seen (Cashman and Marsh 1988; Higgins 2000, 2006; Chakraborti *et al.* 2017; Deb and Bhattacharyya 2018).

CSD was performed on plagioclase crystals of the studied granitoids. The representative thin sections were examined in detail, under the petrographic microscope and photomicrographs of each field of view were taken with at least 30–50% overlap to produce a mosaic of the entire thin section. The plagioclase grains were digitized using the CorelDraw Graphic Suite 2019 software and exported in a B&W uncompressed tiff format (figure 6). The final image is then analyzed using the image analysis software (ImageJ). The image scale was input, and analytical parameters were set to measure crystal length, width, and area. The stereographic conversions of the crystal images were performed using program CSD Correction 1.6 (version 2018) (Higgins 2000). Degree of roundness value was input as 0 and foliation as 0.5 in the software as the samples used in this study contained angular plagioclase grains with magmatic foliation. The 3D crystal aspect ratios were determined using the methodology followed by Higgins (2000). 3D crystal shapes (S: I: L; Short axis: Intermediate axis: Long axis) of different rock-units of Kanara Batholith are given in table 1.

Linear least square regression of the natural logarithm of population density *vs.* crystal size has been plotted to calculate the slope of the curve and intercept values. Cashman and Marsh (1988) suggested that the slope of the CSD curve is related to growth rate and residence time by the equation slope $= -1/Gt$, where G is the crystal's growth rate and t is the residence time. Also, the intercept of the CSD curve is related to the nucleation rate and growth rate by the equation, Intercept $= I/G$, where I is the crystal's nucleation rate.

4.2 *Mineral chemistry*

Well-polished thin sections of the granitoid rocks were examined in detail under the petrographic microscope (Olympus BX-53) available at Ore Research and Exploration Lab, Central University of Kerala, India. The minerals and mineral combinations of interest were then imaged by backscattered electrons (BSE), and their respective mineral chemistry was measured using a JEOL JXA-8230 Superprobe, an Electron Probe Micro-Analyzer (EPMA), housed at the Advanced Facility for Microscopy and Microanalysis, Indian Institute of Science (IISc), Bangalore, India. The thin sections were carbon-coated and analyzed under following conditions, (i) beam diameter of 3 μm; (ii) accelerating potential 15 kV and probe current 12 nA and (iii) count times for the major elements were 10 sec on peaks, 5 sec on each background. Natural silicates and oxide and minerals were used for calibration.

4.3 *Bulk-rock chemistry*

Major oxides were analyzed by X-ray Fluorescence (XRF) technique at CSIR-National Geophysical Research Institute (NGRI), Hyderabad, Telangana, India. Twenty fresh samples representing various Batholith sections were chipped and

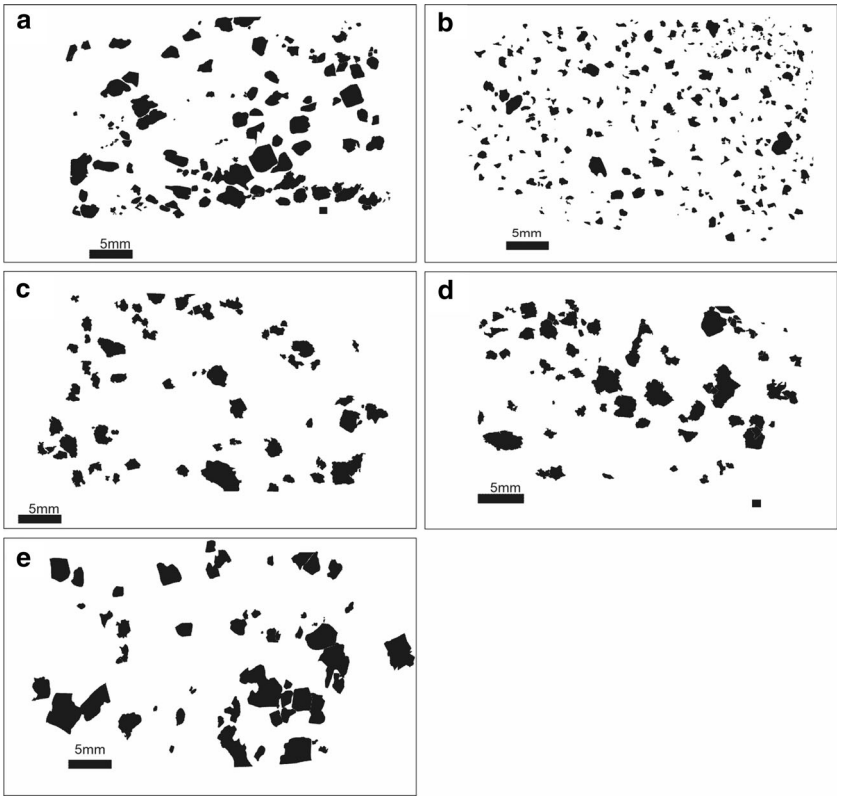

Figure 6. Traced shapes of plagioclase crystals in (**a** and **b**) granodiorites; (**c** and **d**) non-porphyritic granites; and (**e**) porphyritic granites.

Table 1. *Plagioclase CSD results for Kanara batholith granitoids.*

Sample no.	J7	J8	J13	J18	J20
Axial ratio	1:1.5:2.5	1:1.2:3.1	1:1.4:1.8	1:1.5:3.0	1:1.5:3.0
Slope ($-1/Gt$)	–1.0298	–0.7908	–1.0812	–1.5645	–4.2176
Intercept (I/G)	–2.3429	–4.3674	–2.5162	–2.1014	1.6677

powdered with agate mortar to a size of ∼250 mesh. Pressed pellets were prepared by sprinkling finely powdered sample over a boric acid binder filled in aluminium cups and pressing in a 40-ton hydraulic press for the 30 sec. Analyses were performed on a Phillips® MAGIX PRO Model 2440, XRF, with a relative standard deviation of <3% (Krishna *et al.* 2007). International standard JG-2 was used as a standard for measuring the major oxides (supplementary table S1).

In order to measure the trace element concentrations, closed digestion technique was followed. The analyses were carried out in a Nu instruments ATTOM High Resolution Inductively Coupled Plasma Mass Spectrometer, housed at CSIR-NGRI. Homogeneous well-powdered samples of 0.5 g each were taken in Savillex Vials, and 10 ml of an acid mixture containing HF and HNO_3 in 7:3 proportion were added to them. The lids were closed, and vials were heated at 150°C. After 48 hrs, 1–2 drops of perchloric acid ($HClO_4$) were added, and the sample solutions were dried to form a solid residue. 20 ml of an acid mixture containing 1:1 proportion of HNO_3 and Millipore water were added to the sample residue, and the solutions were heated for 1 hr. Next, 5 ml of 1 ppm rhodium solution was used as the internal standard, and the sample solutions were diluted to 250 ml with Millipore water. 5 ml of this solution was further diluted to 50 ml before being analyzed for trace element concentrations. International standard G-2 (United States Geological Survey) was used for

calibration. The data obtained for all analyzed elements are within the RSD limit of <5% (supplementary table S1).

5. Results

5.1 *Crystal size distribution (CSD)*

Most of the samples in the Kanara Batholith exhibit convex-up shaped CSD curves with straight lines. Negative slopes generally characterize the lines. All the studied rock samples are coarse-grained, and the maximum length seen after stereological correction in a plagioclase crystal is 12 mm in the non-porphyritic variant of the granite.

The granodiorites are characterized by a convex-up shaped curvature between grain-sizes 0.25 and 1.75 mm. Further, as the grain size increases, the curve follows a slightly concave-up shaped pattern with the negative slope (figure 7a, b). The convex-up shaped curvature patterns characterize the granites similar to granodiorites. However, the convex-up shaped curvature varies between 0.5 and 4 mm for non-porphyritic granites, and 0.5 and 2 mm for porphyritic granites before the curve becomes a straight line with the negative slope (figure 7c–e).

5.2 *Mineral chemistry*

The electron microprobe analyses of plagioclase, alkali-feldspar, amphibole and biotite are given in tables 2–4.

Plagioclase in the studied rocks is generally oligoclase variant, with the composition varying from $Ab_{76}An_{24}$ to $Ab_{80}An_{20}$ (figure 8a). The plagioclase crystals are devoid of zoning, although, there are feeble variations in their composition from the core to rim. In general, all plagioclase crystals display relatively more albitic rims and less albitic cores.

As noted above, the dominating alkali feldspar in the studied rock types is microcline. Perthites are common. Analysis of microcline shows that the potash feldspar is mostly orthoclase ($Or_{92}Ab_8$ to $Or_{98}Ab_3$) (figure 8a).

Amphiboles are present in the studied granodiorites and are rare or absent in the granites. Analyzed amphibole crystals are characterized by (Ca) > 1.5, (Na) < 0.25 and $\left(\frac{Mg}{Mg+Fe^{2+}}\right) \sim 0.5$ indicating their calcic-magnesian affinity (Yavuz 2007). Based on Leake *et al.* (1997) classification scheme, the studied amphiboles are classified as magnesio-hornblende and ferro-hornblende (figure 8b).

Biotite is the major mafic mineral in the studied rock variants. In the $Mg-(Al+Fe^{3+}+Ti)-(Fe^{2+}+Mn)$ plot (figure 8c) (Foster 1960), the biotite crystals in granodiorite falls on the boundary line between magnesiobiotite and ferrobiotite fields, whereas the biotite crystals in the porphyritic and non-porphyritic granites occupy ferrobiotite fields.

5.3 *Bulk-rock geochemistry*

Twenty representative samples of gneisses (4 nos.), granodiorite (4 nos.) and granites (porphyritic, 5 nos.; non-porphyritic, 7 nos.) from the study area were analyzed for their major and trace element geochemistry. The bulk-rock analytical data for different litho units of the Kanara Batholith are presented in table 5. The following are their salient geochemical characteristics.

Overall, the Kanara Batholith is felsic in composition with a wide range of SiO_2 (64.3–74.4 wt.%), low to moderate K_2O (1.66–4.21 wt.%) and considerably higher Na_2O (4.06–5.71 wt.%) concentrations. They have medium to higher alumina content [$Al_2O_3 > 13$ wt.%] and higher alkali ratio [$Na_2O/K_2O > 1$], characteristic of tonalite–trondhjemite–granodiorites (TTGs) (Champion and Smithies 2003). They have moderate alkali contents [$Na_2O + K_2O = 6.8 - 8.7$ wt.%] with granodiorite occupying the quartz-diorite field and granites (porphyritic and non-porphyritic variants) falling in the granitic field of the total alkali–silica (TAS) classification diagram (figure 9a; Cox *et al.* 1979). In the binary classification diagram of Frost and Frost (2008), the studied granitoids indicate their calc-alkalic to alkali-calcic affinity (figure 9b). The MgO content of the granodiorite (av. 1.96 wt.%) is relatively higher than the granites (av. 0.76 wt.%). The studied granodiorites and granites are characterized by higher mole proportions of Fe than Mg and have Fe* (Fe-number) > 0.5. Hence, they are classified as ferroan (Frost *et al.* 2001). Further, these rocks are characterized by molar $\left[\frac{Na+K}{Al}\right] < 1$ and variable ASI (Alumina Saturation Index), and are thus, classified as metaluminous to slightly peraluminous (figure 9c; Frost *et al.* 2001; Frost and Frost 2008). These features indicate that the studied granitoid rocks are not likely to represent the mantle-derived primary magma

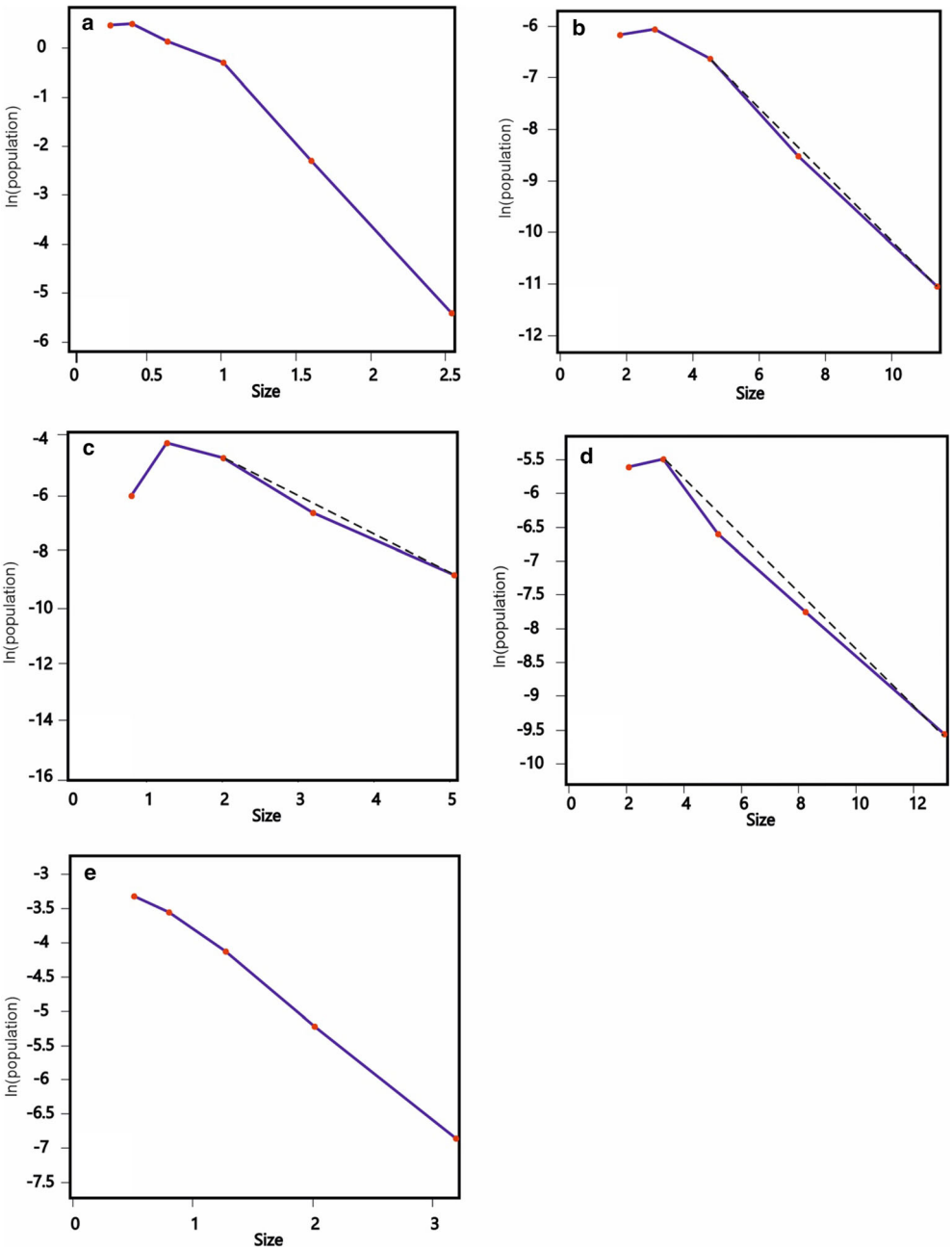

Figure 7. Crystal size distribution curves of (**a** and **b**) granodiorites; (**c** and **d**) non-porphyritic granites; and **(e)** porphyritic granites.

composition. Besides, there is a negative correlation between the SiO_2 and various major oxides (except Na_2O and K_2O; supplementary figure S1) of the studied granodiorites and the granites.

The transitional elements (Cr and Ni) are enriched in granodiorites than the granites (supplementary figure S2). Contrastingly, there is a general enrichment of analyzed large-ion lithophile elements (LILE: Ba, Rb, Sr and Cs), and high-field strength elements (HFSE: Nb, Ta, Zr, Hf and Th) are enriched in granites than the granodiorites. However, overlapping concentrations of certain elements between granodiorites and granites cannot be dismissed (figure 10d, f; supplementary figure S2). In general, the studied granodiorites exhibit low light REE (LREE) fractionation $\left[(\mathrm{La/Sm})_N = 2.21 - 4.55\right]$, with negative to slightly positive europium anomalies $[(\mathrm{Eu/Eu^*}) = 0.55 - 1.90]$ and less-fractionated heavy REE (HREE) $\left[(\mathrm{Gd/Yb})_N = 2.02 - 3.10\right]$. On the contrary, the granites exhibit moderately fractionated LREE $\left[(\mathrm{La/Sm})_N = 5.65 - 10.73\right]$ and less-fractionated HREE $\left[(\mathrm{Gd/Yb})_N = 2.33 - 7.47\right]$, with

Table 2. *Chemical composition (wt.%) and structural formulae of plagioclase.*

Rock type	Granodiorite		Non-porphyritic granite		Porphyritic granite	
Mineral phases	Plagioclase	Alkali feldspar	Plagioclase	Alkali feldspar	Plagioclase	Alkali feldspar
Av. analyses	20	10	35	10	11	10
SiO_2	63.06	64.46	63.57	64.44	63.59	64.53
TiO_2	0.01	0.03	0.01	0.02	0.00	0.01
Al_2O_3	23.68	18.82	22.96	18.88	23.14	18.96
Cr_2O_3	0.01	0.01	0.01	0.01	0.01	0.01
FeO	0.05	0.01	0.07	0.05	0.08	0.03
MnO	0.01	0.02	0.01	0.01	0.02	0.01
MgO	0.00	0.01	0.01	0.02	0.01	0.01
CaO	4.32	0.00	4.67	0.00	4.00	0.01
Na_2O	8.98	0.30	8.74	0.23	9.23	0.80
K_2O	0.11	16.52	0.22	16.59	0.37	15.68
Total	100.24	100.20	100.28	100.25	100.45	100.03
Cations						
Si	2.80	2.99	2.78	2.99	2.80	2.98
Ti	0.00	0.00	0.00	0.00	0.00	0.00
Al	1.22	1.01	1.24	1.02	1.20	1.03
Cr	0.00	0.00	0.00	0.00	0.00	0.00
Fe^{+3}	0.00	0.00	0.00	0.00	0.00	0.00
Fe^{+2}	0.00	0.00	0.00	0.00	0.00	0.00
Mn	0.00	0.00	0.00	0.00	0.00	0.00
Mg	0.00	0.00	0.00	0.00	0.00	0.00
Ca	0.20	0.00	0.22	0.00	0.19	0.00
Na	0.76	0.03	0.74	0.02	0.79	0.07
K	0.01	0.96	0.01	0.97	0.02	0.92
Tot. cat.	5.00	5.00	5.00	5.00	5.00	5.00
Tot. oxy.	8.03	8.01	8.03	8.01	8.00	7.99
An	20.88	0.00	22.52	0.02	18.93	0.05
Ab	78.48	2.73	76.20	2.08	78.99	7.04
Or	0.64	97.27	1.29	97.89	2.08	92.91

negative to slightly positive europium anomalies $[(Eu/Eu^*) = 0.72 - 1.33]$ (figure 10c, e).

Similar major-oxide compositions characterize the basement biotite gneisses surrounding the granitoid pluton. They are metaluminous to slightly peraluminous, ferroan and are generally characterized by lower K_2O, higher Na_2O and alkali ratio. The alumina content is relatively slightly higher than that of the granitoid pluton. The gneisses show considerably similar transitional and large ion lithophile (LIL) element characteristics as that of the granites. However, the HFSE concentration is relatively less than the granodiorite (figure 10b). The moderately fractionated LREE $\left[(La/Sm)_N = 5.07 - 5.97\right]$ and less-fractionated HREE $\left[(Gd/Yb)_N = 2.12 - 5.20\right]$ with a slightly negative to positive europium anomalies $[(Eu/Eu^*) = 0.92 - 2.75]$ characterize the studied gneisses (figure 10a).

6. Geothermobarometry

Al-in-amphibole geobarometer (Anderson and Smith 1995) was used to estimate the pressure of emplacement of the Kanara Batholith. Estimated pressure values for the studied granodiorites ranges between 4.32 and 4.92 kbar (supplementary table S2).

Temperatures of crystallization of Kanara Batholith were calculated using the Ti-in-amphibole (Otten 1984), amphibole–plagioclase (Anderson and Smith 1995), Ti-in-biotite (Henry *et al.* 2005), feldspar-liquid (Putirka 2008) geothermometers.

An average crystallization temperature of 715±15°C was obtained for granodiorites through Ti-in-amphibole thermometer. Similarly, the amphibole–plagioclase thermometer has yielded an average crystallization temperature of 688°C for the studied granodiorites. Crystallization

Table 3. *Chemical composition (wt.%) and structural formulae of amphibole.*

Rock type	Granodiorite
Av. analyses	10
SiO_2	44.93
TiO_2	1.26
Al_2O_3	9.01
Fe_2O_3	0.00
FeO	17.49
MnO	0.45
MgO	10.35
CaO	11.45
Na_2O	0.70
K_2O	1.12
H_2O	3.23
Total	96.77
Si	6.81
Ti	0.14
Al	1.61
Fe^{+3}	0.00
Fe^{+2}	2.22
Mn	0.06
Mg	2.34
Ca	1.86
Na	0.21
K	0.22
H	0.96

temperatures of the studied granites were obtained using Ti-in-biotite geothermometer. An estimated temperature of 625±13°C was obtained for non-porphyritic granites, whereas 650±8°C was obtained for the porphyritic granites.

Further, a temperature of ∼548°C for the granodiorites, ∼569°C for the non-porphyritic granites and ∼598°C for the porphyritic granites were obtained using the feldspar-liquid thermometer (equation 24a of Putirka 2008). Perhaps, these temperatures indicate the lower temperature limits of crystallization.

7. Petrogenesis

7.1 *Relationship between the pluton and the supracrustals of the WGB*

Ramakrishnan and Harinadha Babu (1981) suggested that the Kanara Batholith pluton and the enclosing gneisses form the basement to the volcano-sedimentary sequences of the WGB. The authors also speculated that the pluton could contain younger intrusive components as well. However, Balasubrahmanyan *et al.* (1982) dated the Kanara Batholith porphyritic granites using the Rb–Sr isotopes and obtained an isochron age

Table 4. *Chemical composition (wt.%) and structural formulae of mica.*

Rock type	Granodiorite	Non-porphyritic granite	Porphyritic granite
Av. analyses	10	20	10
SiO_2	37.85	35.76	35.92
TiO_2	1.64	2.78	3.43
Al_2O_3	15.64	16.32	16.62
FeO	16.63	24.19	21.17
MnO	0.33	0.32	0.21
MgO	13.24	6.78	8.27
CaO	0.05	0.00	0.00
Na_2O	0.02	0.02	0.04
K_2O	10.12	9.98	10.09
Cation			
Si	5.69	5.56	5.52
Ti	0.19	0.32	0.40
Al	2.77	2.99	3.01
Fe^{+3}	0.00	0.00	0.00
Fe^{+2}	2.09	3.14	2.72
Mn	0.04	0.04	0.03
Mg	2.97	1.57	1.89
Ca	0.01	0.00	0.00
Na	0.01	0.01	0.01
K	1.94	1.98	1.98
H	2.00	2.00	2.00

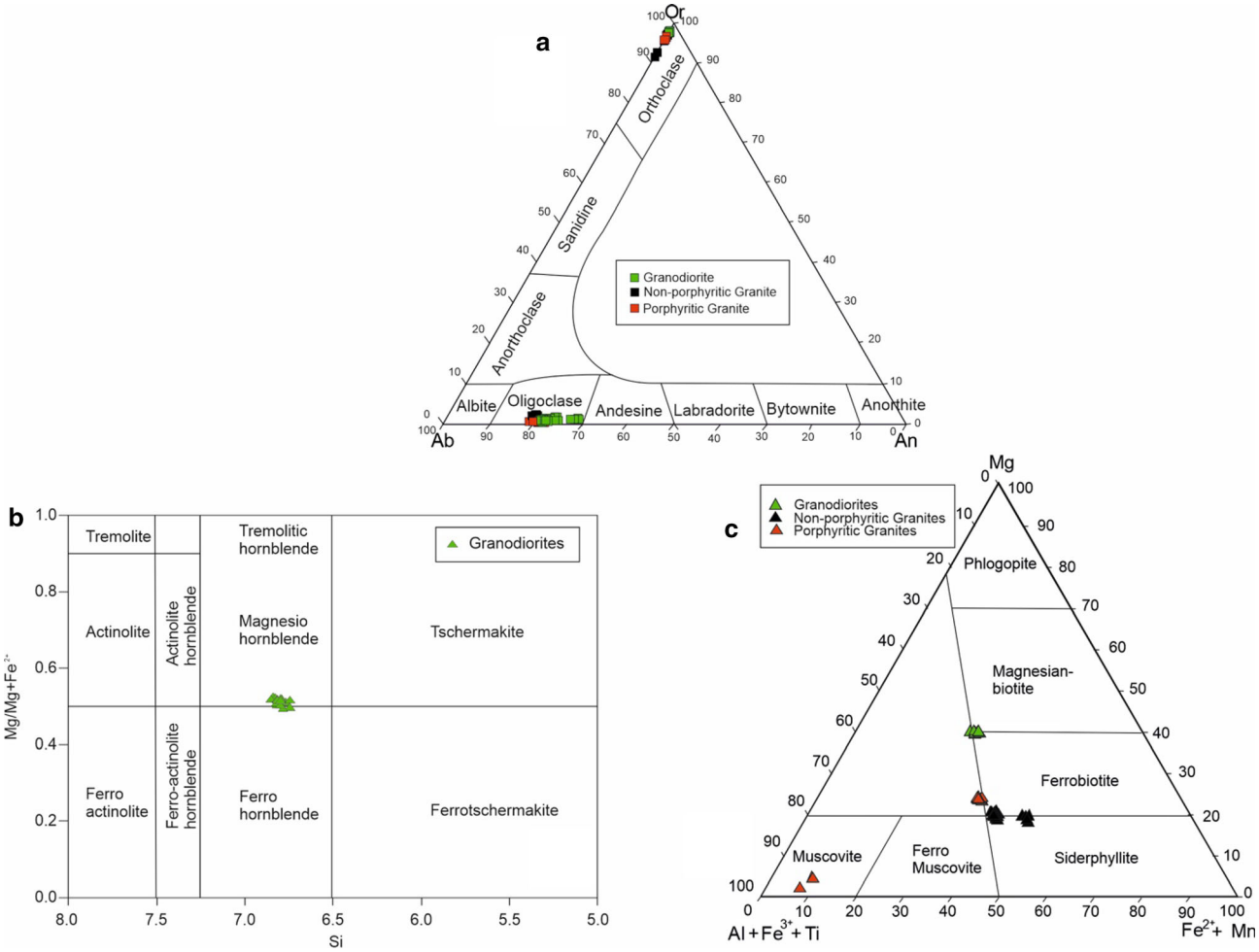

Figure 8. **(a)** Ab–Or–An ternary diagram showing the composition of the studied feldspars; **(b)** classification of amphiboles in the studied granodiorites (Leake *et al.* 1997); and **(c)** classification of micas from the studied granitoids (Foster 1960).

∼2681 Ma. Similarly, the basement gneisses surrounding the Kanara Batholith have been estimated to be ∼3500 to 3200 Ma older based on the K/Ar and Pb/Pb dates (Balasubrahmanyan 1978). Additionally, an Sm–Nd whole-rock isochron age of 3020 Ma have been reported for the basal metavolcanic rocks of the WGB (Drury *et al.* 1983).

In conjunction with the aforesaid isotopic ages and based on our field study in the area, we suggest that the pluton is younger than the supracrustal sequence of the WGB. We base our opinion on the following arguments.

The Kanara Batholith does not show any significant structural deformation signs that affected the basement biotite gneisses and the neighbouring volcano-sedimentary sequences of WGB. The contact between the pluton and the WGB is sharp, which indicates that the pluton was intrusive into the schist belt (figure 3a). Almost perpendicular strike relationship between the granitoid pluton and the supracrustal rocks confirms the cross-cutting relationship. Further, as noted earlier, the pluton exhibits flow banding along the margins with the basement gneisses. Generally, the intensity of these primary flow bands decreases towards the core of the pluton. Besides, characteristics such as (i) occurrences of tongues and apophyses of granites within the adjacent gneisses and the schist belt, (ii) presence of enclaves of schistose rocks along the contact between the pluton and WGB, (iii) intrusive relationship between the granites and the gneisses, and (iv) intense migmatization of the gneisses along the margins with the pluton, point towards the intrusive nature of the pluton.

Therefore, it is inferred that the relative age of a significant proportion of the studied Kanara Batholith is ∼2.6 Ga, making it significantly younger than the oldest known supracrustal unit of the WGB. Further, it is considered that this granitic pluton is an equivalent to the ∼2.6 Ga plutons reported to be intruded into the Dharwar

Table 5. *Bulk-rock geochemical data of Kanara granitoids and surrounding gneisses.*

Sample	J-1	J-2	J-3	J-4	J-5	J-6	J-7	J-8	J-9	J-10	J-11
	Gneisses				Non-porphyritic granites						
SiO_2	71.45	70.10	70.84	72.59	71.12	74.25	68.27	71.03	68.84	68.91	68.63
Al_2O_3	14.15	14.20	13.81	13.57	13.22	13.70	13.93	14.53	15.04	15.19	15.72
Fe_2O_3	1.61	2.02	2.28	1.35	2.87	1.23	4.05	1.71	3.01	2.38	2.69
MnO	0.02	0.03	0.03	0.02	0.04	0.01	0.05	0.03	0.04	0.03	0.03
MgO	0.71	0.74	0.73	0.44	0.79	0.28	1.19	0.79	1.29	0.90	1.19
CaO	1.27	2.85	2.63	2.73	2.51	1.42	2.67	1.90	2.67	2.07	2.49
Na_2O	5.09	5.77	5.93	5.70	5.25	4.19	4.86	4.61	5.41	5.27	5.08
K_2O	3.30	1.36	1.38	1.90	1.66	4.12	1.97	3.45	2.08	2.97	2.24
TiO_2	0.18	0.30	0.27	0.17	0.31	0.13	0.36	0.28	0.38	0.30	0.35
P_2O_5	0.07	0.09	0.08	0.05	0.12	0.02	0.13	0.11	0.13	0.12	0.12
Sc	2.61	3.04	2.91	2.01	3.12	1.78	8.06	2.74	3.86	3.24	3.13
V	18.05	26.38	26.09	13.90	23.18	7.38	34.80	19.62	35.63	27.30	29.78
Cr	13.60	11.70	13.21	10.93	16.84	11.31	21.30	15.03	14.44	13.27	12.76
Co	3.94	4.49	4.22	2.51	5.32	1.56	7.47	4.16	6.29	5.10	5.89
Ni	8.51	7.31	11.42	6.01	6.41	5.76	8.29	7.04	6.64	6.41	6.92
Cu	2.19	3.81	1.65	1.46	1.23	1.33	2.32	1.99	1.73	1.59	1.43
Zn	63	61	31	23	31	30	184	38	43	85	111
Ga	15.07	18.43	17.80	16.10	17.57	15.23	18.08	19.19	19.10	19.28	17.66
Rb	77	32	38	31	59	84	97	118	62	76	65
Sr	228	534	478	433	358	194	302	385	402	446	344
Y	4.76	4.52	3.21	2.00	7.53	3.49	7.03	7.95	6.83	9.34	5.82
Zr	215	186	204	114	246	180	213	247	305	315	305
Nb	4.09	3.28	2.89	1.80	10.44	1.96	8.63	6.09	6.08	5.60	5.74
Cs	0.52	0.48	0.76	0.57	1.54	0.24	3.86	2.22	0.84	0.92	0.97
Ba	397	211	221	349	110	426	187	386	222	350	245
La	14.43	33.74	16.11	8.22	21.12	40.75	20.31	39.44	28.74	38.33	22.61
Ce	28.47	69.25	31.89	16.10	42.23	79.90	40.19	77.46	56.73	75.37	44.38
Pr	2.94	7.67	3.31	1.64	4.47	8.15	4.18	7.93	5.86	7.73	4.54
Nd	9.22	23.90	10.37	5.22	13.71	23.51	12.81	23.02	18.14	22.66	14.32
Sm	1.79	3.55	1.78	0.94	2.35	3.66	2.24	3.40	2.99	3.56	2.36
Eu	0.54	0.76	0.63	0.65	0.61	0.63	0.81	0.72	0.67	0.79	0.72
Gd	1.02	1.80	0.91	0.55	1.50	1.94	1.60	1.90	1.81	2.11	1.51
Tb	0.15	0.23	0.12	0.07	0.22	0.23	0.23	0.26	0.25	0.30	0.21
Dy	0.81	1.11	0.64	0.39	1.25	1.06	1.26	1.40	1.30	1.61	1.11
Ho	0.15	0.14	0.10	0.07	0.23	0.11	0.22	0.25	0.22	0.29	0.19
Er	0.39	0.37	0.27	0.18	0.58	0.28	0.55	0.60	0.54	0.73	0.47
Tm	0.06	0.05	0.04	0.03	0.08	0.04	0.08	0.09	0.08	0.11	0.07
Yb	0.39	0.28	0.25	0.17	0.52	0.21	0.47	0.53	0.48	0.68	0.42
Lu	0.06	0.04	0.04	0.03	0.08	0.03	0.07	0.08	0.07	0.10	0.06
Hf	4.93	3.84	4.59	2.85	5.04	4.60	4.44	5.27	6.39	6.97	6.55
Ta	0.47	0.18	0.18	0.13	2.37	0.14	0.55	0.38	0.35	0.50	0.29
Pb	49.04	48.28	36.61	29.09	36.52	33.97	105.85	29.51	23.33	21.02	24.06
Th	4.59	6.65	2.19	0.94	3.01	20.18	3.83	10.83	10.29	9.52	4.96
U	0.46	0.31	0.32	0.26	0.43	0.93	3.60	3.47	0.62	2.24	0.52

Supergroup of rocks elsewhere in the WDC (Jayananda *et al.* 2013 and references therein).

7.2 *Nature of source*

The 3.5–3.2 Ga old basement biotite gneisses and the surrounding ∼2.6 Ga Kanara Batholith show some similarities in their major oxide composition. The gneisses constitute a significant part of the basement of the Kanara Batholith. Perhaps, these features led Balasubrahmanyan (1978) to propose the Kanara Batholith source to be derived from the partial melting of surrounding gneisses. However, the pluton's specific geochemical characteristics

Table 5. *(Continued.)*

Sample	J-12	J-13	J-14	J-15	J-16	J-17	J-18	J-19	J-20
	Porphyritic granite					Granodiorite			
SiO_2	71.50	73.10	72.54	69.56	72.07	70.25	66.19	64.31	65.80
Al_2O_3	13.44	13.85	13.69	14.92	13.73	14.65	14.21	14.46	14.54
Fe_2O_3	1.56	1.62	1.79	1.35	1.52	2.31	4.44	4.64	3.97
MnO	0.02	0.02	0.02	0.02	0.02	0.03	0.09	0.08	0.05
MgO	0.48	0.50	0.67	0.45	0.53	0.76	2.23	2.46	2.39
CaO	1.62	1.51	1.73	1.79	2.55	2.14	3.95	3.73	2.88
Na_2O	4.06	4.24	4.30	4.70	5.71	4.88	4.77	4.06	4.86
K_2O	4.21	3.97	3.73	3.99	1.66	3.43	2.27	2.98	2.41
TiO_2	0.21	0.19	0.23	0.16	0.19	0.28	0.29	0.36	0.51
P_2O_5	0.05	0.05	0.08	0.06	0.03	0.10	0.21	0.20	0.21
Sc	2.18	2.27	1.92	2.13	1.91	3.04	18.34	15.04	5.92
V	21.35	20.09	24.83	18.00	22.48	23.16	60.63	77.69	49.79
Cr	15.29	12.38	15.51	13.47	17.40	16.78	34.50	38.62	32.88
Co	3.83	3.56	5.37	3.78	4.13	6.32	10.60	11.72	10.31
Ni	6.96	8.56	9.11	7.33	7.43	7.54	8.78	8.68	9.62
Cu	1.57	2.22	3.04	1.78	3.02	2.25	1.80	1.79	2.13
Zn	187.40	48.84	248.85	135.20	111.48	83.46	70.20	74.23	104.86
Ga	15.72	16.92	15.54	17.28	17.87	18.63	21.47	20.73	19.23
Rb	91.06	98.88	92.90	85.98	39.74	94.67	46.58	73.08	66.91
Sr	237.30	215.91	338.40	459.68	439.30	357.51	689.81	681.29	494.49
Y	3.89	4.08	5.91	3.71	3.09	6.04	30.47	26.24	10.93
Zr	248.55	251.45	216.35	142.96	141.80	328.56	223.53	210.25	209.81
Nb	2.07	2.23	2.66	2.28	2.63	5.99	6.76	6.78	4.66
Cs	0.64	0.53	0.68	0.47	0.47	1.54	0.62	1.06	0.82
Ba	397.83	410.02	501.43	713.71	286.61	463.47	335.58	547.61	339.83
La	27.16	57.39	21.62	32.44	53.47	11.21	27.47	33.33	18.22
Ce	52.90	113.19	43.28	62.65	100.21	21.91	65.28	72.23	39.33
Pr	5.33	11.68	4.59	6.21	9.33	2.23	8.87	8.70	4.71
Nd	15.72	33.94	14.03	18.09	26.46	7.33	32.99	31.21	17.14
Sm	2.20	4.49	2.32	2.57	3.13	1.55	7.83	7.05	3.80
Eu	0.69	0.78	0.64	0.79	0.96	0.85	1.18	1.19	0.94
Gd	1.12	2.07	1.43	1.42	1.55	1.21	5.47	4.85	2.45
Tb	0.15	0.25	0.20	0.18	0.18	0.18	0.86	0.75	0.36
Dy	0.78	1.16	1.08	0.88	0.86	1.00	5.02	4.33	2.01
Ho	0.13	0.14	0.19	0.12	0.10	0.19	0.97	0.84	0.35
Er	0.34	0.37	0.49	0.29	0.27	0.48	2.47	2.16	0.88
Tm	0.05	0.06	0.07	0.04	0.04	0.07	0.35	0.31	0.11
Yb	0.34	0.36	0.44	0.22	0.23	0.47	2.18	1.94	0.64
Lu	0.05	0.05	0.06	0.03	0.03	0.07	0.32	0.28	0.09
Hf	5.80	5.67	4.87	3.20	3.15	7.19	4.80	4.50	4.57
Ta	0.11	0.10	0.17	0.10	0.11	0.34	0.42	0.40	0.17
Pb	40.05	24.11	84.29	42.79	37.36	31.66	27.59	30.49	36.30
Th	5.94	14.42	3.55	10.22	13.25	4.45	3.55	3.43	2.13
U	0.77	0.82	0.65	0.45	0.42	0.81	0.64	0.49	0.47

noted in this study, such as relatively lower Sr and Ba concentrations and lack of significant negative europium anomaly, suggest that the hypothesis of the derivation of their magmas by partial melting of the gneissic source rocks alone is not consistent. Also, lack of significant correlation among the major oxides of the gneisses and the granodiorites (supplementary figure S1) does not support the partial melting of gneisses alone as a process that could have resulted in the formation of the studied granitic melt.

Several studies have suggested that the Late Archean granites could be derived from the interaction between mantle-derived magmas

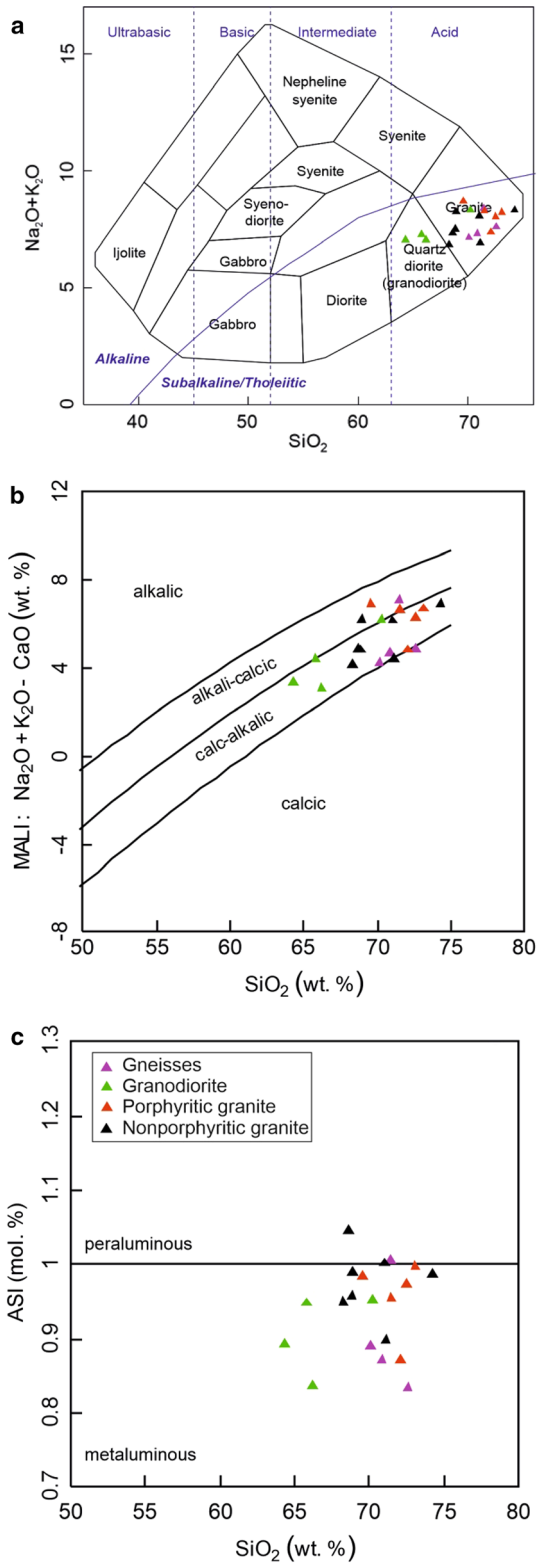

Figure 9. **(a)** Total alkali-silica classification diagram (Cox *et al.* 1979); **(b)** modified alkali-lime index (MALI) *vs.* SiO_2 binary plot (Frost and Frost 2008); **(c)** alumina saturation index (ASI) *vs.* SiO_2 binary plot (Frost and Frost 2008).

(sanukitoids) and crustal melts (Almeida *et al.* 2010; Dey *et al.* 2016; Elangovan *et al.* 2019; Dey and Moyen 2020; Jayananda *et al.* 2020). Such melts are usually calc-alkaline to alkali-calcic, metaluminous, potassic with low Na_2O and high Ba and Sr concentrations. However, the studied granitoids are enriched in Na_2O and are characterized by relatively lower Ba (<1000 ppm) than in the expected melt product derived from the mixing between the sanukitoid magmas and the crustal melts. The possibility of the melt, which gave rise to the pluton, being derived from the crustal derived magmas interaction is also ruled out due to unique sodic nature and relatively low Rb and Th contents and K_2O/Na_2O ratios of the studied granitoids (Laurent *et al.* 2014).

Late-Archean granitoid rocks formed through interaction between magmas of multiple sources are incredibly heterogeneous. Such rocks are difficult to define on geochemical criteria alone since their sources and petrogenetic mechanism differs from one place to another (Laurent *et al.* 2014). They usually result from the interactions between the melts generated by the partial melting of sanukitoids and the felsic crustal rocks. Few examples of such granitoids include Mashashane, Mashishimale, Matlala and Moletsi plutons of the Pietersburg block (Laurent *et al.* 2014), as well as several granitoids in the Superior Province (Whalen *et al.* 2004) and the Dharwar Craton of south India (Moyen *et al.* 2001; Jayananda *et al.* 2006). The Kanara Batholith consists predominantly of sodic plagioclase, K-feldspar and quartz with biotite as the dominant mafic mineral. Primary muscovite is absent while hornblende is occasional. The textural characteristics obtained for the studied granodiorites using CSD patterns indicate the role of magma mixing during its genesis. The key geochemical features of the studied granitoids such as their calc-alkaline to alkali-calcic and metaluminous-slightly peraluminous nature, as well as high SiO_2 (>64.3 wt.%), ferromagnesian oxides ($1 \leq Fe_2O_3+MgO+MnO+TiO_2 \leq 8$ wt.%) and variable K_2O/Na_2O (0.3–1.04) ratios suggest that these rocks were derived from the interaction of the multiple sources. The studied rocks are characterized by low Rb content, negative Ba anomaly and positive Sr anomaly in the primitive mantle normalized multi-element diagram (figure 10) which suggests a crustal felsic source (gneisses+metasediments) (Almeida *et al.* 2010; Laurent *et al.* 2014). Further, they are depleted in Nb, a common feature of rocks derived from a crustal source (Whalen *et al.* 1996). However, they are also characterized by higher Sr/Y and Ba/Rb ratios similar to the rocks derived from the partial

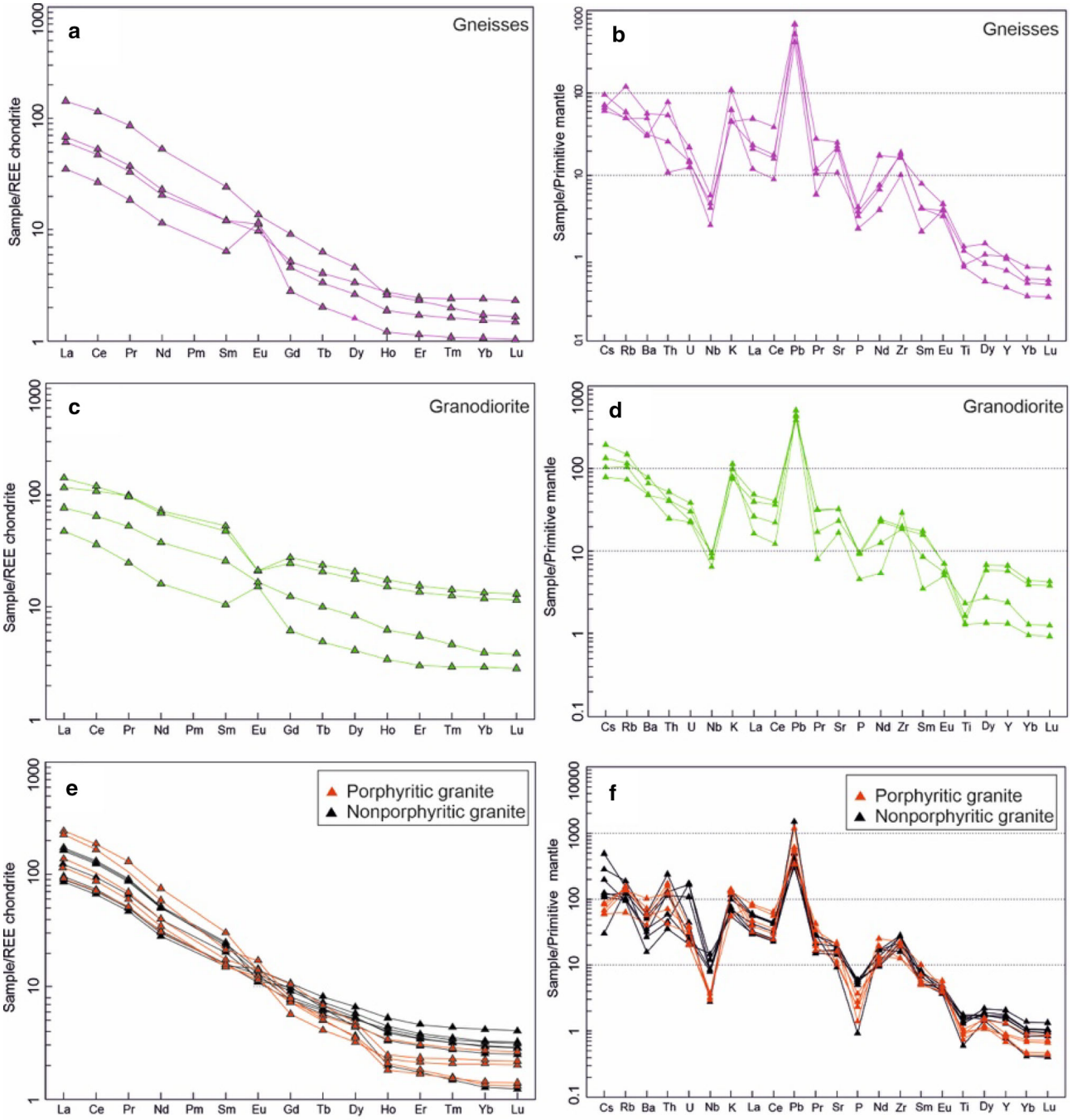

Figure 10. Chondrite-normalized REE patterns (Boynton 1984) and primitive-mantle normalized multi-element patterns (Sun and McDonough 1989) of the studied granitoids.

melting of gneissic rocks (Laurent *et al.* 2014). The REE patterns are moderate to highly fractionated ($9 \leq (La/Yb)_N \leq 165$) with variable Eu anomalies ($0.6 \leq (Eu/Eu^*) \leq 1.3$). These characteristics are also indicative of a rock derived from a heterogeneous magma source.

Based on the arguments described above and evidence, we interpret that the source magmas of the studied granitoids were derived from the interaction between (i) a melt derived from the partial melting of the surrounding basement biotite gneisses and (ii) a melt derived from the partial melting of the crustal felsic rocks (gneisses+metasediments). As mentioned earlier, the lithostratigraphic succession of the study area indicates the basement for the Kanara Batholith and the Late Archean Supracrustal enclaves (WGB) is made up of the biotite gneisses and the Early Archean supracrustal enclaves (Sargur Group). The voluminous distribution of biotite gneisses makes them the prime suspect for the origin

of the plutonic magma. Further, we propose that the additional melt derived from the partial melting of the early Archean metasediments interacted with the gneissic derived melt at shallow to mid-crustal levels at pressures $\lesssim 5$ kbar before crystallization.

In order to test the association of biotite gneisses and metasediments as a source for the studied granitoids, a magma mixing model is carried out. The select incompatible trace element concentrations of metasediments of the Sargur Group (Naqvi 1983) and biotite gneisses (this study) are used to test the mixing hypothesis. A mixture involving 95% biotite gneisses and 5% metasediments is tested. The resulting residue (Kanara Granitoids) composition curve fits perfectly well with the incompatible trace element curve of the biotite gneisses of the study area (supplementary figure S3a). In the absence of metasedimentary source, the fits for the incompatible trace elements between the biotite gneisses and granitoids are generally poor and distorted (supplementary figure S3b). Hence, the role of a minor metasedimentary source cannot be ruled out in the genesis of the studied granitoids.

7.3 *Depth of emplacement*

The mineral-chemical evidence such as uniform crystal composition, a single generation of plagioclase crystals and development of subsolvus feldspars (perthites) indicate that the studied pluton crystallized in an equilibrium condition within a static magma chamber without any remarkable fluctuation in the P–T conditions. The granodiorites have yielded crystallization pressure of 4.32–4.92 kbar which is less than the pressures attained by the supracrustal rocks of the WGB (6–8 kbar; Janardhan *et al.* 1982; Raith *et al.* 1983; Raase *et al.* 1986). Assuming an average crustal specific gravity of 3.0 g/cm^3, an approximate emplacement depth of crystallization is estimated between $\sim$15 and $\sim$17 km. Further, the crystallization temperatures of the pluton vary between 715±15° and 548±15°C, with a gradual decrease of crystallization temperatures from the granodiorites to the non-porphyritic granites. The maximum crystallization temperature estimated for the pluton is less than the metamorphic temperatures attained by the supracrustal sequences of the WGB (>750°C; Janardhan *et al.* 1982; Raith *et al.* 1983; Raase *et al.* 1986). Further, as noted earlier, all along the contact margin of the pluton and the WGB (and biotite gneiss), enclaves of supracrustal (and gneissic) rocks are seen (figure 3b). These supracrustal enclaves show similar schistose characteristics as that of its parent in the WGB.

All these features indicate that the studied granitoid magma was intruded into the gneissic country rocks and the supracrustal sequences of the WGB at a depth of $\sim$15–17 km, before it began to crystallize in a static magma chamber at temperatures <715±15°C.

7.4 *Magma chamber processes*

Bulk-rock geochemical evidence of the studied granitoids highlights the role of magma mixing in the origin of the granitoids of the Kanara Batholith. As noted earlier, chemically similar melts generated by the partial melting of the gneisses and the crustal felsic (mainly metasedimentary) rocks were involved in the process of magma mixing. Hence, significant mineralogical or textural characteristics indicating the magma mixing process, such as resorbed grain boundaries, mantling of high-temperature mineral over the low-temperature mineral and mixed apatite morphologies, seen in the case of mafic–felsic magma interactions, are not expected to be seen in the studied granitoid rocks (Wyllie *et al.* 1962; Hibbard 1991; Vernon 2018). This is mainly because, the interaction between the chemically similar melts usually results in the formation of the felsic microgranular enclaves and intricate zoning patterns in feldspars (Alves *et al.* 2009) as a result of the variable melt temperatures. Though significant zoning patterns are not seen in the feldspars, the presence of occasional felsic microgranular enclaves (figure 3f) whose mineralogical composition is similar to the studied non-porphyritic granites is attributed to the magma mixing process. Further, the nature of the CSD curves obtained for the granodiorites points towards the role of magma mixing in the genesis of the studied pluton.

The bulk-rock geochemical data indicate a negative correlation between the SiO_2 and various major oxides (TiO_2, Fe_2O_3, MgO and CaO) of the studied granodiorites and granites (supplementary figure S1) which suggests the granites were the products of the fractional crystallization of the granodioritic melt. The general decrease in compatible elements and an increase in incompatible elements from granodiorite to granite (supplementary figure S2) further corroborates the role of fractional crystallization in the genesis of the studied granites.

Occasional mantling of biotite over hornblende in the studied granodiorites and the complete absence of amphiboles in the granites indicate the evolution of the felsic magma to generate relatively less mafic mineral phases as crystallization proceeded along with a progressive increase in the hydrous content. The convex-up shaped CSD curves, with straight and occasionally curved lines characterized by the negative slopes, of plagioclase indicate that the magma-mixing, along with the textural coarsening during fractionation, played a significant role in the growth of the crystals within the magma chamber (Higgins 2011). Further, the variation of plagioclase crystal size between 0.5 and 12 mm can be attributed to either crystallization at different crustal levels or textural coarsening mechanism (Chakraborti *et al.* 2017). Crystallization at different crustal levels results in variable plagioclase compositions. However, in the studied granitoids, the plagioclase crystals are characterized by uniform composition (granodiorite $Ab_{77}An_{80}$; granite $Ab_{76}An_{78}$), which supports the role of textural coarsening in the growth of the mineral crystals within the felsic magma chamber.

8. Conclusion

A combined field, textural, mineralogical and bulk-rock geochemical study has been carried out on the Kanara Batholith granitoid situated in the western part of the WDC. These granitoids are classified as granodiorites and granites based on their modal mineral abundances. Further, the granites are of two variants: porphyritic and non-porphyritic. A meagre amount of hornblende is seen in the granodiorites, while it is absent in the granites. Biotite forms the predominant mafic mineral phase in the studied granitoids. Textural investigation indicates the importance of textural coarsening in the growth of mineral crystals of the granitoids. Thermobarometric studies suggest that the granites have been emplaced and crystallized at pressures between 4.32 and 4.92 kbar and temperatures between 548±15 and 715±15°C. It is also evidenced that the granitoid magma intruded into the gneissic country rocks and the supracrustal sequences of the WGB at a depth of ∼15 to 17 km. Bulk-rock geochemical evidence suggests that the source magmas of the studied granitoids were derived from the interaction between (i) a melt derived from the partial melting of the basement biotite gneisses and (ii) a melt derived from the partial melting of the early Archean metasedimentary rocks that forms the enclaves within the basement biotite gneisses. This source magma interacted in due course to generate the hybrid felsic magma that resulted in the Kanara Batholith formation. We suggest that the interaction of the melt took place at shallow to mid-crustal levels at pressures $\lesssim$ 5 kbar before the crystallization began.

Acknowledgements

Dr Ram Mohan and Dr Srinivasa Sarma of CSIR-National Geophysical Research Institute, Hyderabad and Dr Sajeev Krishnan of Indian Institute of Science (IISc), Bengaluru are thanked for extending analytical facilities. Mr Bikash Nayak, Mr Bilal Ibn Ashraf, Mr Githin Mon and Mr Subhendu Pradhan were greatly helpful during the field work and sample preparation. CKB acknowledges the financial support received from the Science and Engineering Research Board (SERB), India in the form of Early Career Research (ECR) Grant (ECR/2016/001449). CKB is thankful to Dr Kumar Batuk Joshi for the discussions during the preparation of the manuscript. The authors are grateful to the Head, Department of Geology, Central University of Kerala, for providing infrastructural facilities to carry out this study.

Author statement

JKP: Formal analysis, resources, software, writing – original draft. CKB: Conceptualization, methodology, visualization, supervision, funding acquisition, writing – original draft, review and editing, supervision. RC: Formal analysis and software.

References

Almeida Jd A C, Dall'Agnol R, Dias S B and Althoff F J 2010 Origin of the Archean leucogranodiorite–granite suites: Evidence from the Rio Maria Terrane and implications for granite magmatism in the Archean; *Lithos* **120** 235–257.

Alves A, de Assis Janasi V, Simonetti A and Heaman L 2009 Microgranitic enclaves as products of self-mixing events: A study of open-system processes in the Mauá granite, São Paulo, Brazil, based on *in-situ* isotopic and trace elements in plagioclase; *J. Petrol.* **50** 2221–2247.

Anderson J L and Smith D R 1995 The effects of temperature and fO_2 on the Al-in-hornblende barometer; *Am. Mineral.* **80** 549–559.

Balasubrahmanyan M N 1978 Geochronology and geochemistry of Archean tonalitic gneisses and grantites of south Kanara district, Karnataka state, India; In: *Archean geochemistry* (eds) Windley B F and Naqvi S M, pp. 57–77.

Balasubrahmanyan M N, Bishui P K, Chandy K C, Gupta S N, Jana N K, Paul D K and Prasad R 1982 New Rb–Sr age of Kanara granite, south Kanara district, Karnataka state; *J. Geol. Soc. India* **23** 402–405.

Boynton W 1984 Cosmochemistry of the Rare Earth Elements: Meteorite Studies; In: *Devel. Geochem.* **2** 63–114.

Cashman K V and Marsh B D 1988 Crystal size distribution (CSD) in rocks and the kinetics and dynamics of crystallization. II: Makaopuhi lava lake; *Contrib. Mineral. Petrol.* **99** 292–305.

Chadwick B, Vasudev V and Hegde G 2000 The Dharwar craton, southern India, interpreted as the result of late Archaean oblique convergence; *Precamb. Res.* **99** 91–111.

Chadwick B, Vasudev V, Hegde G and Nutman A P 2007 Structure and shrimp U/Pb zircon ages of granites adjacent to the Chitradurga Schist Belt: Implications for Neoarchaean convergence in the Dharwar craton, southern India; *J. Geol. Soc. India* **69** 5–24.

Chakraborti T M, Ray A and Deb G K 2017 Crystal size distribution analysis of plagioclase from gabbro-anorthosite suite of Kuliana, Orissa, Eastern India: Implications for textural coarsening in a static magma chamber; *Geol. J.* **52** 234–248.

Champion D and Smithies R 2003 Archaean granites; In: *Magmas to mineralization,* The Ishihara Symposium, Geoscience, Australia, pp. 19–24.

Chandan Kumar B and Ugarkar A G 2017 Geochemistry of mafic–ultramafic magmatism in the Western Ghats belt (Kudremukh greenstone belt), Western Dharwar craton, India: Implications for mantle sources and geodynamic setting; *Int. Geol. Rev.* **59** 1507–1531.

Chardon D, Jayananda M and Peucat J J 2011 Lateral constrictional flow of hot orogenic crust: Insights from the Neoarchean of south India, geological and geophysical implications for orogenic plateau; *Geochem. Geophys. Geosyst.* **12**.

Condie K 2014 Growth of continental crust: A balance between preservation and recycling; *Mineral. Mag.* **78** 623–638.

Condie K C, Belousova E, Griffin W and Sircombe K N 2009 Granitoid events in space and time: Constraints from igneous and detrital zircon age spectra; *Gondwana Res.* **15** 228–242.

Cox K, Bell J D and Pankhurst R 1979 *The Interpretation of Igneous Rocks*, William Clowes, London, Britain.

Deb T and Bhattacharyya T 2018 Interaction between felsic granitoids and mafic dykes in Bundelkhand craton: A field, petrographic and crystal size distribution study; *J. Earth Syst. Sci.* **127** 102.

Devaraju T, Viljoen R, Sawkar R and Sudhakara T 2009 Mafic and ultramafic magmatism and associated mineralization in the Dharwar craton, southern India; *J. Geol. Soc. India* **73** 73–100.

Dey S 2013 Evolution of Archaean crust in the Dharwar craton: The Nd isotope record; *Precamb. Res.* **227** 227–246, https://doi.org/10.1016/j.precamres.2012.05.005.

Dey S, Halla J, Kurhila M, Nandy J, Heilimo E and Pal S 2016 Geochronology of Neoarchean granitoids of the NW eastern Dharwar Craton: Implications for crust formation; *Geol. Soc. Spec. Publ.* **449** 89–121.

Dey S and Moyen J-F 2020 Archean granitoids of India: Windows into early Earth tectonics – An introduction; *Geol. Soc. Spec. Publ.* **489** 1–13.

Drury S A, Holt R W, Van Calsteren P C and Beckinsale R D 1983 Sm–Nd and Rb–Sr ages for Archaean rocks from western Karnataka, South India; *J. Geol. Soc. India* **24** 454–459.

Elangovan R, Asokan A D, Pandit D and Mohan M R 2019 Magma chamber processes and geodynamic implications of the Pithora pluton, Bastar Craton, Central India; *Geol. J.* **55(4)** 2738–2759.

Foster M D 1960 Interpretation of the composition of trioctahedral micas; *U.S. Geol. Surv., Prof. Pap.* **354-B** 11–49.

Frost B R, Barnes C G, Collins W J, Arculus R J, Ellis D J and Frost C D 2001 A geochemical classification for granitic rocks; *J. Petrol.* **42** 2033–2048.

Frost B R and Frost C D 2008 A geochemical classification for feldspathic igneous rocks; *J. Petrol.* **49** 1955–1969.

Henry D J, Guidotti C V and Thomson J A 2005 The Ti-saturation surface for low-to-medium pressure metapelitic biotites: Implications for geothermometry and Ti-substitution mechanisms; *Am. Mineral.* **90** 316–328.

Hibbard M J 1991 *Petrography to Petrogenesis*; Prentice Hall, London, UK.

Higgins M D 2000 Measurement of crystal size distributions; *Am. Mineral.* **85** 1105–1116.

Higgins M D 2006 *Quantitative textural measurements in igneous and metamorphic petrology*; Cambridge University Press.

Higgins M D 2011 Quantitative petrological evidence for the origin of K-feldspar megacrysts in dacites from Taapaca Volcano, Chile; *Contrib. Mineral. Petrol.* **162** 709–723.

Janardhan A, Newton R and Hansen E 1982 The transformation of amphibolite facies gneiss to charnockite in southern Karnataka and northern Tamil Nadu, India; *Contrib. Mineral. Petrol.* **79** 130–149.

Jayananda M, Aadhiseshan K, Kusiak M A, Wilde S A, Sekhamo K U, Guitreau M, Santosh M and Gireesh R 2020 Multi-stage crustal growth and Neoarchean geodynamics in the eastern Dharwar craton, southern India; *Gondwana Res.* **78** 228–260.

Jayananda M, Chardon D, Peucat J J and Capdevila R 2006 2.61 Ga potassic granites and crustal reworking in the western Dharwar craton, southern India: Tectonic, geochronologic and geochemical constraints; *Precamb. Res.* **150** 1–26.

Jayananda M, Guitreau M, Thomas T T, Martin H, Aadhiseshan K, Gireesh R, Peucat J J and Satyanarayanan M 2019 Geochronology and geochemistry of Meso-to-Neoarchean magmatic epidote-bearing potassic granites, western Dharwar craton (Bellur–Nagamangala–Pandavpura corridor), southern India: Implications for the successive stages of crustal reworking and cratonization; *Geol. Soc. London, Spec. Publ.* **489** SP489–2018.

Jayananda M, Peucat J J, Chardon D, Rao B K, Fanning C and Corfu F 2013 Neoarchean greenstone volcanism and continental growth, Dharwar craton, southern India: Constraints from sims U–Pb zircon geochronology and Nd isotopes; *Precamb. Res.* **227** 55–76.

Jayananda M, Santosh M and Aadhiseshan K 2018 Formation of Archean 3600–2500 Ma continental crust in the Dharwar craton, southern India; *Earth-Sci. Rev.* **181** 12–42.

Krishna A K, Murthy N N and Govil P K 2007 Multi-element analysis of soils by wavelength-dispersive X-ray fluorescence spectrometry; *Atom. Spectrosc.* **28(6)** 202–214.

Larson M and Randolph A 1971 *Theory of particulate processes: Analysis and techniques of continuous crystallization*; Academic Press, New York.

Laurent O, Martin H, Moyen J F and Doucelance R 2014 The diversity and evolution of late-Archean granitoids: Evidence for the onset of 'modern-style' plate tectonics between 3.0 and 2.5 Ga; *Lithos* **205** 208–235.

Leake B E, Woolley A R, Arps C E, Birch W D, Gilbert M C, Grice J D, Hawthorne F C, Kato A, Kisch H J and Krivovichev V G 1997 Nomenclature of amphiboles: Report of the subcommittee on amphiboles of the international mineralogical association commission on new minerals and mineral names; *Mineral. Mag.* **61** 295–321.

Marsh B D 1988 Crystal size distribution (CSD) in rocks and the kinetics and dynamics of crystallization; *Contrib. Mineral. Petrol.* **99** 277–291, https://doi.org/10.1007/BF00375362.

Mohan R M, Asokan A D and Wilde S A 2020 Crustal growth of the Eastern Dharwar Craton: A Neoarchean collisional orogeny? *Geol. Soc. London, Spec. Publ.* **489**, https://doi.org/10.1144/SP489-2019-108.

Moyen J F, Martin H and Jayananda M 2001 Multi-element geochemical modelling of crust–mantle interactions during late-Archaean crustal growth: The Closepet granite (south India); *Precamb. Res.* **112** 87–105.

Moyen J F, Martin H, Jayananda M and Auvray B 2003 Late Archaean granites: A typology based on the Dharwar craton (India); *Precamb. Res.* **127** 103–123.

Mukherjee S, Ghosh G, Das K, Bose S and Hayasaka Y 2017 Geochronological and geochemical signatures of the granitic rocks emplaced at the north-eastern fringe of the Eastern Dharwar Craton, South India: Implications for late Archean crustal growth; *Geol. J.* **53(5)** 1781–1801.

Nicoli G 2020 Water budget and partial melting in an Archean crustal column: Example from the Dharwar Craton, India; *Geol. Soc. London, Spec. Publ.* **489**, https://doi.org/10.1144/SP489-2018-88.

Otten M T 1984 The origin of brown hornblende in the Artfjället gabbro and dolerites; *Contrib. Mineral. Petrol.* **86** 189–199.

Peucat J J, Jayananda M, Chardon D, Capdevila R, Fanning C M and Paquette J L 2013 The lower crust of the Dharwar craton, southern India: Patchwork of Archean granulitic domains; *Precamb. Res.* **227** 4–28.

Putirka K D 2008 Thermometers and barometers for volcanic systems; *Rev. Mineral. Geochem.* **69** 61–120.

Raase P, Raith M, Ackermand D and Lal R 1986 Progressive metamorphism of mafic rocks from greenschist to granulite facies in the Dharwar craton of south India; *J. Geol.* **94** 261–282.

Raith M, Raase P, Ackermand D and Lal R 1983 Regional geothermobarometry in the granulite facies terrane of south India; *Earth Environ. Sci. Trans. Roy. Soc. Edinburgh* **73** 221–244.

Ramakrishnan M and Harinadha Babu P 1981 Western Ghats belt; In: *Early Precambrian supracrustals of southern Karnataka* (eds) Ramakrishnan M and Nath J S, *Geological Survey of India*, pp. 147–161.

Ramakrishnan M and Vaidyanadhan R 2010 *Geology of India* (vol. 1 & 2); GSI Publications 2, Bengaluru.

Ranjan S, Upadhyay D, Abhinay K and Srikantappa C 2020 Paleoarchean and Neoarchean Tonalite–Trondhjemite–Granodiorite (TTG) and granite magmatism in the Western Dharwar Craton, southern India: Implications for Archean continental growth and geodynamics; *Precamb. Res.*, https://doi.org/10.1016/j.precamres.2020.105630.

Streckeisen A 1974 Classification and nomenclature of plutonic rocks recommendations of the IUGS sub-commission on the systematics of igneous rocks; *Geol. Rundschau* **63** 773–786.

Sun S and McDonough W 1989 Chemical and isotopic systematics of oceanic basalts: Implications for mantle composition and processes; *Geol. Soc. London, Spec. Publ.* **42** 313–345.

Tait J, Zimmermann U, Miyazaki T, Presnyakov S, Chang Q, Mukhopadhyay J and Sergeev S 2011 Possible juvenile Paleoarchean TTG magmatism in eastern India and its constraints for the evolution of the Singhbhum Craton; *Geol. Mag.* **148(2)** 340–347.

Vernon R H 2018 *A practical guide to rock microstructure*; Cambridge University Press.

Whalen J B, Jenner G A, Longstaffe F J, Robert F and Gariepy C 1996 Geochemical and isotopic (O, Nd, Pb and Sr) constraaints on A-type granite petrogenesis based on the Topsails igneous suite, Newfoundland Appalachians; *J. Petrol.* **37(6)** 1463–1489.

Whalen J B, Percival J A, McNicoll V J and Longstaffe F J 2004 Geochemical and isotopic (Nd–O) evidence bearing on the origin of late-to post-orogenic high-K granitoid rocks in the western superior province: Implications for late Archean tectonomagmatic processes; *Precamb. Res.* **132** 303–326.

Wyllie P, Cox K and Biggar G 1962 The habit of apatite in synthetic systems and igneous rocks; *J. Petrol.* **3** 238–243.

Yavuz F 2007 Winamphcal: A windows program for the ima-04 amphibole classification; *Geochem. Geophys. Geosyst.* **8**.

Corresponding editor: N V Chalapathi Rao